frontiers | Frontiers in Earth Science

TYPE Original Research
PUBLISHED 05 May 2023
DOI 10.3389/feart.2023.1188142

OPEN ACCESS

EDITED BY
Gilad Antler,
Ben-Gurion University of the Negev,
Israel

REVIEWED BY
Chin Yik Lin,
University of Malaya, Malaysia
Or M. Bialik,
University of Malta, Malta

*CORRESPONDENCE
Fumito Shiraishi,
fshirai@hiroshima-u.ac.jp

RECEIVED 17 March 2023
ACCEPTED 18 April 2023
PUBLISHED 05 May 2023

CITATION
Shiraishi F, Akimoto T, Tomioka N, Takahashi Y, Matsumoto R and Snyder GT (2023), Microbial traces found in microdolomite associated with seep-related shallow gas hydrate.
Front. Earth Sci. 11:1188142.
doi: 10.3389/feart.2023.1188142

Microbial traces found in microdolomite associated with seep-related shallow gas hydrate

Fumito Shiraishi[1]*, Takayuki Akimoto[1], Naotaka Tomioka[2], Yoshio Takahashi[3], Ryo Matsumoto[4] and Glen T. Snyder[5]

[1]Earth and Planetary Systems Science Program, Hiroshima University, Hiroshima, Japan, [2]Kochi Institute for Core Sample Research, X-star, JAMSTEC, Kochi, Japan, [3]Department of Earth and Planetary Science, The University of Tokyo, Tokyo, Japan, [4]Gas Hydrate Research Laboratory, Meiji University, Kawasaki, Kanagawa, Japan, [5]Atmosphere and Ocean Research Institute (AORI), The University of Tokyo, Kashiwa, Chiba, Japan

Recently, microdolomite grains with a diameter of about 30–150 μm were discovered within seep-related shallow gas hydrate in the eastern margin of the Japan Sea, and the preliminary assumption has been that their formation is mediated by microbially secreted extracellular polymeric substances (EPS). To verify this interpretation, the present study investigates the characteristics of minerals and organic matter inside the microdolomite grains. Observation by polarizing microscopy reveals that the microdolomite grains generally consist of combinations of distinct cores and external cements. The cores are mostly dark or cloudy and their abundance does not show clear depth dependence, while the external cements are generally isopachous in the shallow part and polygonal in the deeper portions. To further clarify the characteristics of these cores and external cements, thin-foil sections were prepared from two major types of microdolomite, one with a dark core and polygonal external cement, and one with a cloudy core and isopachous external cement. These thin-foil sections were then analyzed by scanning transmission X-ray microscopy (STXM) and transmission electron microscopy (TEM). In the dark core, fibriform pores of about 100 nm diameter were observed to be closely related with amorphous calcium carbonate (ACC) and carboxy groups, likely created by heterogeneous nucleation on microbial EPS surfaces. The polygonal external cement is composed of monocrystalline dolomite, representing slow crystal growth in the deeper part where hydrate formation is less active. On the other hand, the observed cloudy core and the isopachous external cement are, respectively, composed of scattered and accumulated rhombohedral dolomite crystals, presumably resulting from homogeneous nucleation in saline pockets of rapidly growing hydrate and subsequent crystal accumulation on the surface of spherical oil films.

KEYWORDS

ACC, dolomite, EPS, gas hydrate, Japan Sea, microbial carbonate, microhabitat

1 Introduction

The Joetsu Basin in the eastern margin of the Japan Sea hosts a number of areas with extensive shallow methane deposits and various related phenomena, including well-developed gas chimneys, active methane seeps and readily observed hydroacoustic plumes (Aoyama et al., 2004; Matsumoto et al., 2017). The seafloor in these areas hosts

pock marks and large depressions associated with methane hydrate collapse (Matsumoto et al., 2009) as well as authigenic carbonate crusts and nodules composed of aragonite and Mg-rich calcite (Hiruta et al., 2014; Zhang et al., 2019). Recently, a new type of authigenic mineral, microdolomite, with a diameter of about 30–150 μm was discovered from hydrate-bearing cores drilled in this area (Snyder et al., 2020a).

Dolomite [$CaMg(CO_3)_2$] is a carbonate mineral, of which the euhedral crystal is rhombic (e.g., Petrash et al., 2017). Dolostones composed mainly of dolomite are widespread in the geological record, while the occurrence of dolomite is limited in modern marine settings despite the general observation that the seawater is highly supersaturated for dolomite. This is mainly because the crystallization of dolomite under relatively low temperature/pressure conditions is inhibited by various factors, including strong hydration of Mg^{2+} and the presence of sulfate ion (e.g., James and Jones, 2016). Dolostones in the geological records are generally thought to have formed by weakening these inhibition factors particularly during diagenesis, and dolomite precipitated as cement or replaced primary $CaCO_3$ minerals (e.g., Tucker and Wright, 1990). On the other hand, sulfate-reducing bacteria has been reported to form dolomite primarily (Vasconcelos et al., 1995), which is accomplished by metabolic SO_4^{2-} removal and dolomite nucleation on the organic matrix (Warthmann et al., 2000).

The primary growth of microdolomite grains directly associated with microbial activity is thought to occur in a number of settings, such as shallow marine lagoon sediments in Brazil (Vasconcelos and McKenzie, 1997; Bahniuk et al., 2015) and Eocene and Quaternary petroleum seep sites in Kuwait (Gunatilaka, 1989). Like other dolomite-forming settings, the voids which develop inside of massive gas hydrate accumulations are also considered favorable sites for dolomite formation because the microenvironments in close contact with gas hydrate are also limited in SO_4^{2-} or sulfate-free due to anaerobic methane oxidation (AMO). In addition, water removal via rapid hydrate growth produces brine where hydration of Mg^{2+} is weakened. Snyder et al. (2020a) also suggested that oil-covered brine in the hydrates provides microhabitat for oil-metabolizing microorganisms and their secreted extracellular polymeric substances (EPS) supply suitable substrate for dolomite precipitation. One of the promising approaches to verify this interpretation is to detect carboxy groups and amorphous calcium carbonate (ACC) in the microdolomite. This is because the crystallization process of carbonate minerals on organic molecules is thought to proceed as follows: ACC nanoparticles are formed in the liquid phase, they accumulate on negatively charged organic matter such as EPS containing acidic groups (particularly carboxy groups characterized by a relatively low dissociation constant), and the crystalline phase nucleates from ACC precursors (Pouget et al., 2009). Carboxy groups may also facilitate dolomite precipitation by dehydration of Mg^{2+} (Roberts et al., 2013). Although ACC is less stable than crystalline phases, it is stabilized when it coexists with negatively charged organic matter (Addadi et al., 2003; Obst et al., 2009; Xu et al., 2018). Therefore, if microdolomite was formed by nucleation on negatively charged EPS, traces such as carboxy groups and ACC are expected to be remained inside.

These traces can be detected, for example, by analyzing a thin-foil sections with scanning transmission X-ray microscopy (STXM) and transmission electron microscopy (TEM). Actually, these methods were applied for investigating the calcification process of cyanobacteria, and revealed that the traces of ACC nanoparticles remained around EPS containing carboxy groups (Shiraishi et al., 2020). This study, therefore, aims to verify the involvement of microbial EPS in microdolomite formation by applying these methods. By doing so, this study will reveal the actual processes of primary dolomite formation by microorganisms and the characteristics of their products, which would provide essential information for interpreting dolostones in the geological past.

2 Materials and methods

The study site is the Umitaka Spur located in the Joetsu Basin, the eastern margin of the Japan Sea. Hydrocarbons in the region are presumably derived from gas and oil sourced from the organic-rich upper-Miocene Nanatani Formation located at several kilometers depth (Muramoto et al., 2007; Nyugen et al., 2016). The gas has subsequently migrated towards the surface forming gas chimney structures, shallow methane hydrate accumulations and active seeps (Hiruta et al., 2009; Matsumoto et al., 2009; 2017; Snyder et al., 2020b). In the course of exploration in this area, Snyder et al. (2020a) discovered microdolomite in oil-bearing hydrates and described the basic characteristics of these small mineral grains distributed within the hydrate matrix. The microdolomite grains often show dark internal cores, in which saline fluid and even the trace of microorganisms are occasionally hosted. In addition, microdolomite has positive $\delta^{13}C$ values (from +15.60 to +41.63‰ at Umitaka Spur), which is similar to the values of dissolved inorganic carbon in the interstitial water (from −4.9 to +41.4‰ at Umitaka Spur) while it is quite distinct from the values of hydrate (from −36.6 to −34.6‰ at Umitaka Spur) and methane derived authigenic carbonates (MDACS; from −46.8 to −5.6 at Umitaka Spur). Based on these results, Snyder et al. (2020a) interpreted that the rapid hydrate growth led to the exclusion of oily and saline pockets, in which the organotrophic microorganisms metabolize the oil and produce EPS to form spherulitic microdolomite. Among the microdolomite samples examined by Snyder et al. (2020a), this study focuses on a subset contained in a core drilled at the margin of large pock mark in the central western portion of Umitaka Spur (UTCW).

These microdolomite grains were collected by dissociating the hydrate, isolating the solid phase by centrifugation, washing twice with deionized water, rinsing with ethanol, and drying at 40 °C. Sample splits of those studied by Snyder et al. (2020a) were used for our current study as well as several not yet analyzed. The morphological features of the microdolomite grains observed in each sample were first observed using plane polarized light (PPL) with a polarizing microscope (Eclipse LV100POL, Nikon). From this observation, several types of microdolomite were recognized as described later, and samples containing two typical types were selected for further examinations (samples G122 and AMI01 collected respectively from 17.23 mbsf and 66.27 mbsf). These two samples were embedded in resin (LR White, London Resin) at 60°C for 24 h, and then conventional thin sections of about 50 μm thick were prepared. From these thin sections, thin-foil sections (~150–200 nm thick) were prepared using a focused ion

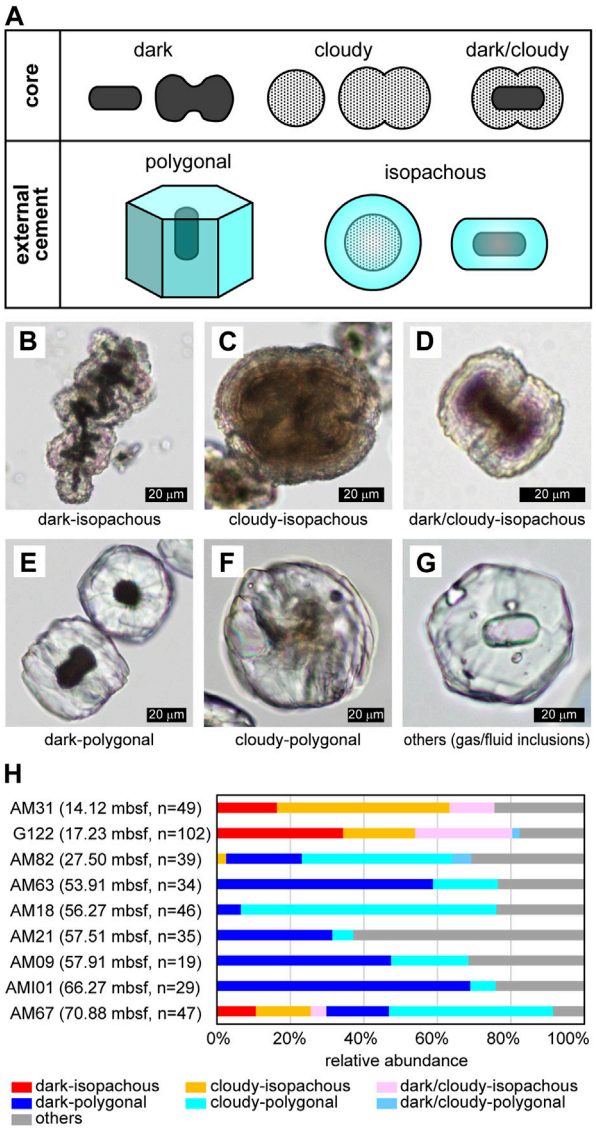

FIGURE 1
Morphological variations of microdolomite. **(A)** Summary of typical core and external cement types. **(B)**–**(G)** Typical combinations of core and external cement. PPL images. **(B)** Combination of dark core and isopachous external cement. Many bacilliform dark cores are observed. Sample G122. **(C)** Combination of cloudy core and isopachous external cement. It looks like conjoining of four spherical cores. Fine concentric laminae are sometimes recognized in the core and cement. Sample G122. **(D)** Combination of dark/cloudy core and isopachous external cement. The dark core is bacilliform, but the surrounding cloudy part is dumbbell-shaped. Fine laminae are recognizable in the external cement. Sample G122. **(E)** Combination of dark core and polygonal external cement. The grain on the upper right is a view of the hexagonal prism from above, and the faint streaks extending radially from the core are recognizable. On the other hand, the grain in the lower left is a view of hexagonal prism from the side, and the faint parallel to wedge-shaped streaks are recognizable. The elongating directions of the hexagonal prism and the bacilliform core are the same. Sample AM101. **(F)** Combination of cloudy core and polygonal external cement. The core is slightly dumbbell-shaped. Sample AM09. **(G)** An example of other types exhibiting polygonal external cement with some gas or fluid inclusions. Sample AM63. **(H)** Depth distribution of core-cement combinations. The sampling depth is also shown in parentheses.

beam (FIB) apparatus (SMI-4050, Hitachi) with a 30 keV Ga ion beam. Before ion milling, carbon was deposited on the sample surface for protection.

Thin-foil sections were observed using STXM and TEM mostly based on the methods of Shiraishi et al. (2020). Briefly, this study used STXM established at BL19A beamline of KEK-PF (Tsukuba, Japan). STXM is a type of X-ray microscopy using synchrotron radiation, which is capable of high-resolution mapping of the valency and chemical state of elements in the soft X-ray region. In this study, calcium L-edge and carbon K-edge NEXAFS (near edge X-ray absorption fine structure) spectra and images were obtained, and these spectra and images were analyzed using aXis 2000 software (Hitchcock, 2009). Whole images of thin-foil sections were acquired at several energy steps (345.0, 348.1, 348.5 and 352.6 eV for calcium; 280.0, 288.6, 290.3, and 301.5 eV for carbon), and their overviews were generated using the RGB composite method after subtracting the backgrounds (345.0 eV and 280.0 eV for calcium and carbon, respectively). Around the central part of microdolomite, image stacks were obtained and composition maps were generated using representative spectra with the singular value decomposition (SVD) method. Spectra of calcite, aragonite, and ACC reported by Shiraishi et al. (2017); Shiraishi et al. (2020) were used for references. In addition, reference spectra were acquired from dolomite, albumin (as a representative of protein), agarose (as a representative of saccharide without carboxy group), D-glucuronic acid (as a representative of saccharide with carboxy group), as well as artificial materials contained in the thin-foil sections, namely, LR White resin and carbon deposition. Thin-foil sections were further observed with TEM (JEM-ARM200F, JEOL) operated at an accelerating voltage of 200 kV. Apertures for obtaining selected-area electron diffraction (SAED) patterns were 0.25, 0.6, and 1.1 μm in diameter. In addition, high-angle annular dark field (HAADF) images were generated in scanning TEM (STEM) mode.

3 Results

3.1 Morphological variations of microdolomite

The morphology of microdolomite grains was described previously through the microscopic observation of external morphology and the degree to which microcrystalline spheroidal aggregates are conjoined, ranging from single grains to dumbbell, chain, and cauliflower-shapes (Snyder et al., 2020a). In this study we consider both the internal and external characteristics of the microdolomite grains and classify them according to the combinations of distinct cores and external cements. The internal cores of the microdolomite aggregates can be dark, or opaque, or they can be cloudy but still capable of transmitting light in microscopic section, or they can be a combination of cloudy and dark. The external, cemented portion of the microdolomites can be polygonal or isopachous (Figure 1A). Examples of these combinations include bacilliform black cores in PPL surrounded by isopachous external cement forming a chain aggregate

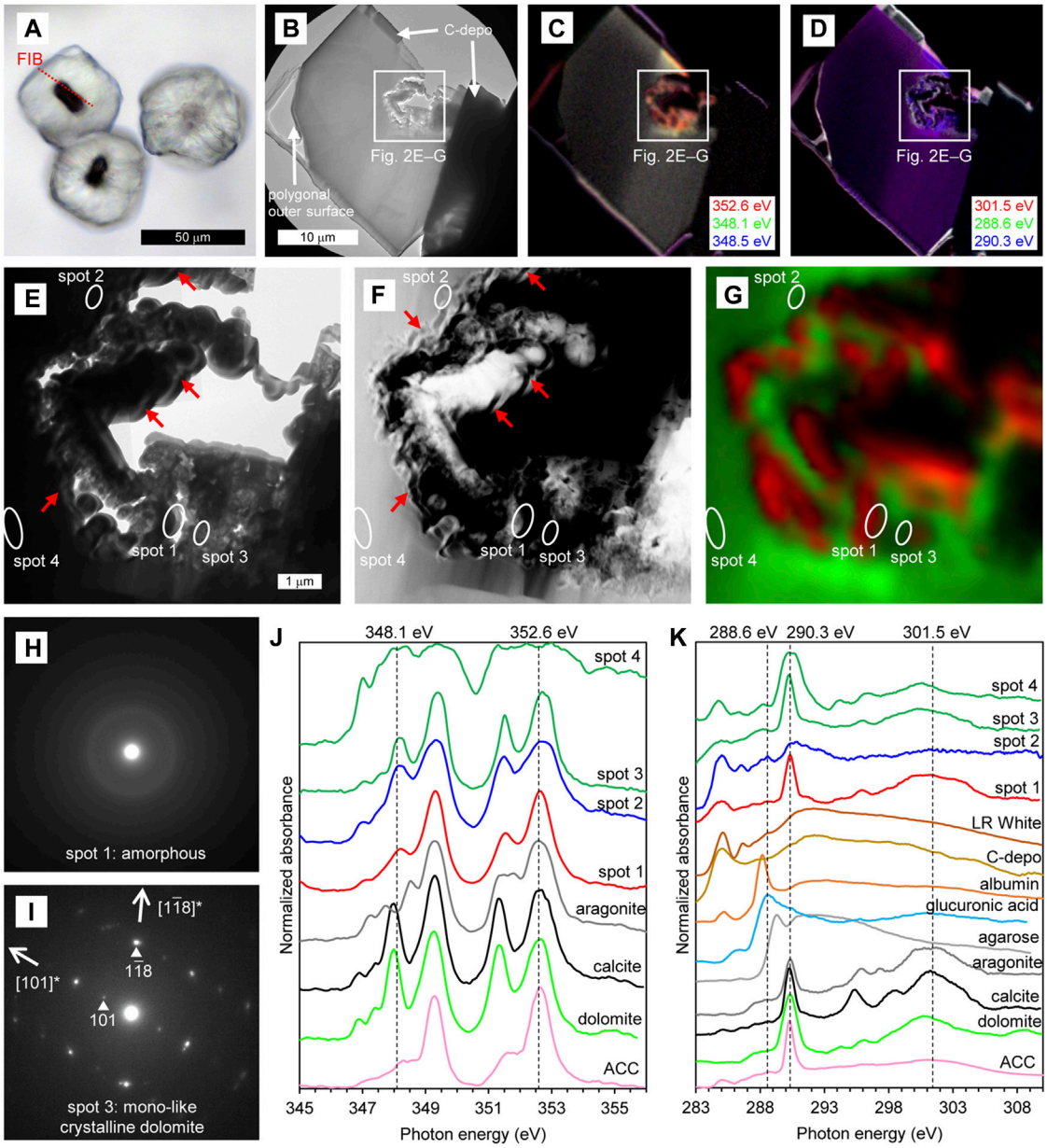

FIGURE 2
Characteristics of dark–polygonal type. **(A)** PPL image of the thin section. The red dashed line indicates the location of the thin-foil section prepared by FIB. **(B–D)** Overviews of the thin-foil section, showing BF-TEM image **(B)** and STXM-based compositional images for Ca **(C)** and C **(D)**. The upper margin of the thin-foil section is protective carbon deposition (C-depo). **(E–G)** Magnified region from **(B–D)**, showing a BF-TEM image **(E)**, HAADF-STEM image **(F)**, and STXM-based SVD mapping **(G)**. Spots for NEXAFS spectra and SAED patterns are indicated. Red arrows in **(E)** and **(F)** represent some examples of fibriform pores. **(H and I)** SAED patterns taken from spots 1 **(H)** and 3 **(I)**, showing the presence of amorphous phase and mono-like crystalline dolomite, respectively. **(J)** Ca NEXAFS spectra of four sample spots and reference materials. The spectrum of spot 1 is representative of the red areas in **(G)**. The spectra of spots 3 and 4 are representative of the green areas in **(G)**, exhibiting thin and thick parts of the dolomite, respectively. X-ray absorbance at spot 4 is saturated due to relatively thick sample section. **(K)** C NEXAFS spectra of four sample spots and reference materials. X-ray absorbance of spot 4 is also somewhat saturated due to relatively thick sample section.

(Figure 1B), cloudy-cores surrounded by isopachous cement (Figure 1C), dark/cloudy cores surrounded by isopachous cement forming a paired dumbbell structure (Figure 1D). In general, the isopachous cement is relatively transparent and conformably fringes the core morphology with a slight pinching in the case of dumbbell pairs. The microdolomites with polygonal surfaces all present transparent external cement and may have dark cores (Figure 1E) although others have cloudy cores (Figure 1F). Others have no apparent core (Figure 1G), yet may present either fluid or gas inclusions.

The relative abundance of each core and cement combination is shown for samples listed from shallow to deep (Figure 1H), along

with the number of grains counted for each sample. Isopachous cement was observed to be dominant at the depth above ~14–17 mbsf, while polygonal cement was found to be dominant in the deeper gas hydrates. On the other hand, the relative abundance of dark, dark/cloudy, and cloudy core types did not show a clear depth dependence.

In order to further characterize the cores and external cements, two distinct, yet fairly typical, microdolomite grains were selected for STXM and TEM observations: a dark-polygonal type (sample AMI01) recovered from gas hydrate at 66.27 mbsf and a cloudy-isopachous type (sample G122) recovered from relatively shallow gas hydrate at 17.23 mbsf.

3.2 Observation of thin-foil section: dark-polygonal type

For the dark-polygonal type, a thin-foil section was prepared so that the section included both the core and the external cemented portion (Figure 2A). However, since the core seemed to be weak when subjected to the Ga ion beam, FIB processing was stopped even though the section was relatively thick (approximately 200–300 nm). Bright-field (BF) TEM imagery shows that the obtained thin-foil section contains a cross-section of about 1/3 of the external cement in addition to the core, and that the core has cavities, while the external cement is rather structureless (Figure 2B). In the STXM-based compositional images for Ca (Figure 2C), the core is displayed in red because X-ray absorption at 348.1 eV is less significant than that at 352.6 eV, as is characteristic for ACC and aragonite (Figure 2J). On the other hand, the external cement is displayed in yellow because the absorptions both at 348.1 eV and 352.6 eV were significant (although the color was not prominent due to strong self-absorption by the relatively thick section), which is characteristic for dolomite and calcite (Figure 2J). In the STXM-based compositional images for C (Figure 2D), the external cement is displayed in purple because the absorptions both at 290.3 eV and 301.5 eV were significant. Absorptions at 290.3 eV and 301.5 eV (and also two peaks between ca. 294.0 eV and 298.5 eV) correspond, respectively, to π^* and σ^* carbonate resonances, and their relative intensities are sensitive to crystal orientation rather than to mineral species (Metzler et al., 2008; Brandes et al., 2010; Gilbert et al., 2011). Therefore, the uniform purple color in the external cement suggested that it was composed of single crystal of carbonate mineral at least across the observable range.

In a more detailed observation around the core, BF-TEM image shows that wavy/spiral fibriform pores of about 100 nm wide are observable near the boundary between the cavity and the mineral (e.g., arrows in Figure 2E). These fibriform pores are more clearly observed in the HAADF-STEM image (e.g., arrows in Figure 2F). STXM-based SVD mapping (Figure 2G) showed Ca NEXAFS spectra characteristic of ACC surrounding the fibriform pores (red areas including spot 1), and the spectra characteristic of dolomite and calcite in the surrounding area (green areas including spots 2–4). In the SAED patterns, the area showing the Ca NEXAFS spectrum characteristic of ACC was amorphous (spot 1, Figure 2H). On the other hand, in the area showing the spectra characteristic of dolomite and calcite, the SAED pattern is indicative of mono-like crystalline dolomite (i.e., dolomite with a slightly different crystal orientation; spot 3, Figure 2I). In the C NEXAFS spectra, a weak absorption peak at around 288.6 eV is recognizable, particularly near the fibriform pores (spot 2 in Figure 2K), was as is characteristic of carboxy groups exemplified by the spectrum of D-glucuronic acid (Benzerara et al., 2004; Mitsunobu et al., 2016; and references therein). Weak absorption peaks are also recognizable around 288.2 eV near the fibriform pores (spot 2 in Figure 2K) and surrounding dolomite (spots 3 and 4 in Figure 2K), which is characteristic of protein as exemplified by the spectrum of albumin. On the other hand, the peaks around 284.9 eV and 286.5 eV in the spectra of spots 1–4 also appeared in the resin and carbon deposition, suggesting that these peaks originated from artificial materials.

3.3 Observation of thin-foil section: cloudy-isopachous type

For the cloudy-isopachous type, the thin-foil section was also prepared so that the section included both the core and the externally cemented areas (Figure 3A). BF-TEM image shows that the obtained thin-foil section contains a cross-section of about 1/4 of the spherical core and the external cement, and that the scattered minerals in the core are divided by a dense mineral layer (Figure 3B). The external cement was also consisted of similar but thicker mineral layer. The STXM-based compositional images for Ca (Figure 3C) are largely displayed in light-yellow indicating significant absorptions at both 348.1 eV and 352.6 eV, was as is characteristic of dolomite and calcite (Figure 3J). On the other hand, the rim of the scattered minerals in the core is displayed as reddish, indicating a relatively weak absorption at 348.1 eV as described above. In the STXM-based compositional images for C (Figure 3D), the section is largely displayed in red due to relatively significant absorption at 301.5 eV, indicating that the crystal orientation is similar within the observable range. However, the lower left area of the thin-foil section and some of the scattered minerals in the core are displayed in purple due to significant absorption both at 290.3 eV and 301.5 eV, indicating their different crystal orientation.

In a more detailed observation around the core, BF-TEM (Figure 3E) and HAADF-STEM (Figure 3F) images shows that the minerals scattered in the core were generally rhombohedrons of about 0.1–2 μm in size, and that the dense mineral layer in the core and external cement are composed of aggregates of rhombohedral minerals. STXM-based SVD mapping (Figure 3G) shows Ca NEXAFS spectra characteristic of dolomite and calcite in most part of the core and external cement (green areas including spots 2 and 3). On the other hand, as with the overviewing compositional images for Ca, the rim of the scattered minerals in the core exhibits a spectrum with relatively weak absorption at 348.1 eV (red areas including spot 1), but this absorption peak is more significant if compared with the spectrum of ACC (Figure 3J). This is the crystal field peak, which is significant for crystals like dolomite, and is less significant for less-ordered crystals such as polycrystalline dolomite, and is insignificant for disordered ACC (Politi et al., 2008; Gong et al., 2012). In fact, the SAED pattern indicates that the area showing relatively weak absorption at 348.1 eV is polycrystalline dolomite (spot 1, Figure 3H). On the other hand, in the area showing Ca NEXAFS spectra characteristic of dolomite and calcite, the SAED pattern indicates monocrystalline dolomite (spot 2, Figure 3I). The C NEXAFS spectra does not show any significant peaks other than the resin, carbon deposition, and carbonate (Figure 3K).

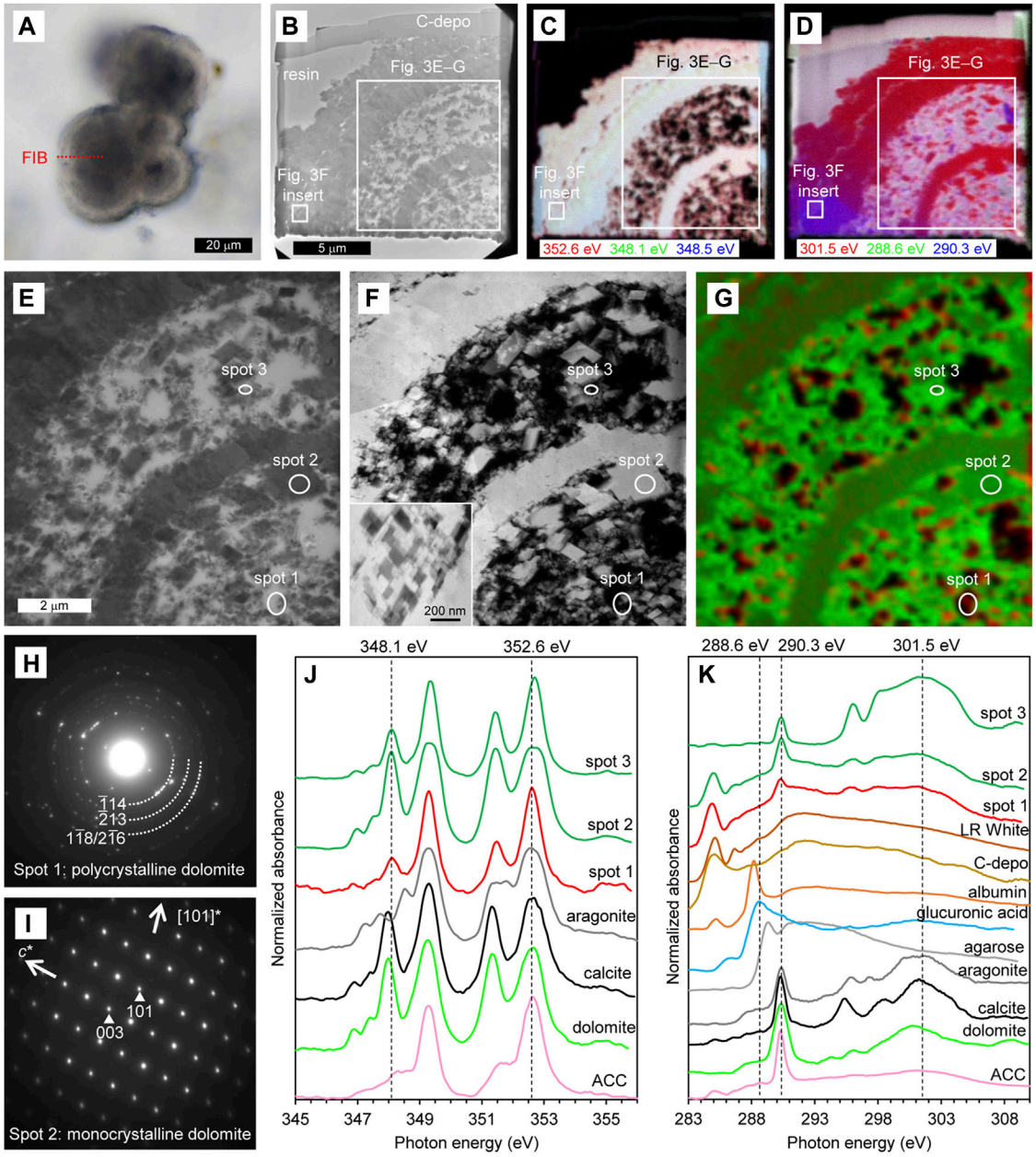

FIGURE 3
Characteristics of cloudy–isopachous type. **(A)** PPL image of the thin section. The red dashed line indicates the location of the thin-foil section prepared by FIB. **(B–D)** Overviews of the thin-foil section, showing BF-TEM image **(B)** and STXM-based compositional images for Ca **(C)** and C **(D)**. The upper margin of the thin-foil section is protective carbon deposition (C-depo). **(E–G)** Magnified region from **(B–D)**, showing a BF-TEM image **(E)**, HAADF-STEM image **(F)**, and STXM-based SVD mapping **(G)**. Spots for NEXAFS spectra and SAED patterns are indicated. An inserted image in F is a magnification of the external cement, as shown in **(B–D)**. **(H, I)** SAED patterns taken from spots 1 **(H)** and 2 **(I)**, showing the presence of polycrystalline and monocrystalline dolomite, respectively. **(J)** Ca NEXAFS spectra of three sample spots and reference materials. The spectrum of spot 1 is representative of the red areas in **(G)**. The spectra of spots 2 and 3 are representative of the green areas in **(G)**, exhibiting thick and thin parts of the dolomite, respectively. **(K)** C NEXAFS spectra of three sample spots and reference materials.

4 Discussion

The observations of this study reveal the typical characteristics of cores and external cements that constitute the microdolomite. In the dark-polygonal type, fibriform pores of about 100 nm in diameter are closely related with ACC and carboxy groups in the core areas, which are surrounded by a polygonal external cement composed of monocrystalline dolomite (Figure 2). While these pores were considerably smaller than typical prokaryotic cells (mostly 0.5–2.0 μm in diameter; e.g., Black, 2005), their size and morphology were similar to hydrogels of polysaccharides and EPS incorporated in carbonate minerals. For example, Li and Estroff (2007) reported that the fibriform pores of about 60–360 nm wide were formed in calcite if the fibers of agarose gel, a neutral

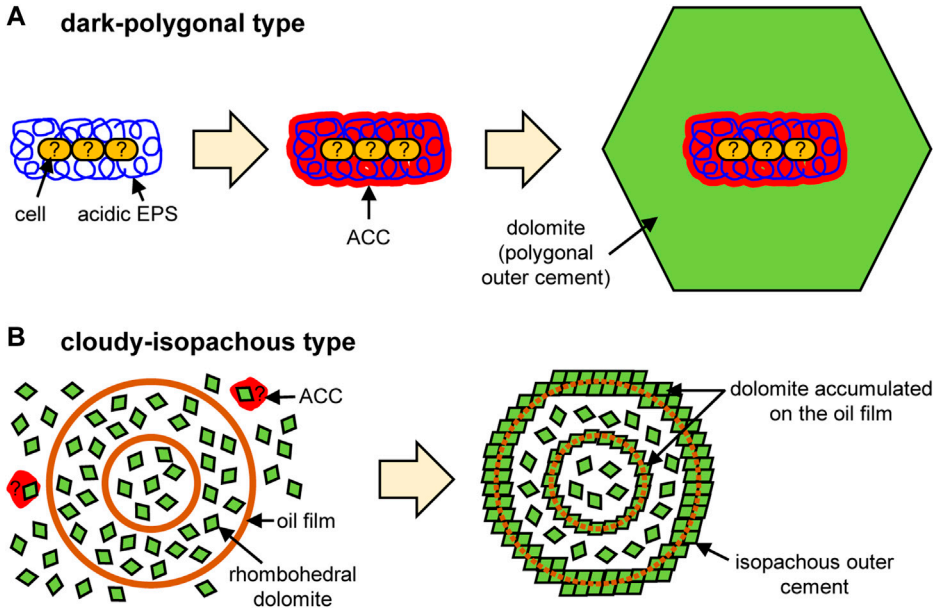

FIGURE 4
Conceptual models of microdolomite formation for **(A)** dark-polygonal type and **(B)** cloudy-isopachous type.

polysaccharide, were incorporated into the crystal. Yin et al. (2020) also reported similar results using both agarose and microbial acidic EPS. Therefore, it is likely that the fibriform pores in the dark core represent microbial EPS containing carboxy groups, which have induced heterogeneous nucleation (i.e., nucleation on the foreign surface; De Yoreo and Vekilov, 2003) of dolomite crystals via ACC precursors. The dark core of the examined microdolomite is bacilliform, but it is about 8 μm wide and 17 μm long, which is considerably larger than a single prokaryotic cell (Figure 2A). Alternative possibilities may be an assembly of multiple cells, or an aggregate of EPS separated from the cells. In the former case, it is possible that cells were degraded naturally by diagenesis or artificially during FIB processing, because there is no morphological evidence of cells in the thin-foil section despite the presence of protein around the core. Such EPS-producing microorganisms may be oil-metabolizing organotrophs such as Flavobacteria, as suggested by the previous study (Snyder et al., 2020a), and the dark color of the core may come from the coexisting oil. In any case, acidic EPS with or without cells would provide the necessary nucleation sites for dolomite, after which the crystal growth of dolomite can occur abiotically in the supersaturated saline pockets (Figure 4A).

The cloudy-isopachous type microdolomite does not present observable fibriform pores, ACC, or carboxy groups. Instead, the core consists mainly of scattered rhombohedral dolomite (Figure 3), which is capable of dispersing transmitted light to produce the observed cloudy appearance. Scattered rhombohedral dolomite also aggregates into spherical crusts to form core-dividing dense layers and isopachous external cement (Figure 3). Such scattered euhedral crystals suggest the occurrence of homogeneous nucleation (i.e., nucleation within the bulk solution; De Yoreo and Vekilov, 2003). Since homogeneous nucleation requires much higher supersaturation of solute than heterogeneous nucleation (Stumm and Morgan, 1996), it is conceivable that the rapid hydrate growth significantly concentrates the remaining water, in which hydration of Mg^{2+} has weakened and a conspicuous amount of rhombohedral dolomite has crystallized in this brine. Although ACC precursors may be involved in their nucleation, such traces would not be stabilized due to the lack of EPS containing carboxy groups (Addadi et al., 2003; Obst et al., 2009; Xu et al., 2018). On the other hand, in order for rhombohedral crystals to accumulate and form a hollow spherical crust (though rhombohedral crystals are scattered inside), a spherical template is required. A possible candidate is an oil-covered brine as suggested by the previous study (Snyder et al., 2020a). Although the traces of oil film were not detected in the course of this study, it is likely that the oil has been lost because ethanol was used for washing and resin embedding. If nanocrystals (e.g., the inserted image of Figure 3F) had accumulated on the surface of such a spherical template, a spherical crust would have been formed. In fact, it has become clear that crystallization by attachment of particles such as nanocrystals is a general phenomenon (De Yoreo et al., 2015). If the spherical oil film was double-layered, a concentric structure like the sample in this study would have been formed (Figure 4B).

In this study, the observations using polarizing microscopy have revealed that the microdolomite grains exhibit distinct cores and external cements. The high-resolution observations by TEM and STXM further reveal the formation processes of these unusual grains which are potentially ubiquitous in saline, sulfate-limited environments. We hope that these data will provide the essential information for understanding the origin of small dolomite grains found in the thin sections of geological samples. To our knowledge, there have been no similar studies carried out yet, but small dolomite grains have been reported from other areas. For example, Sadooni et al. (2010) described rounded and rhombic dolomite with a diameter of ~5 μm from sabkha in Abu Dhabi, and Perri et al. (2018) described

rhombic dolomite with a diameter of 1–20 μm from sabkha in Qatar. They are smaller in diameter and different in shape if compared to the microdolomite of this study. This suggests that they have different origins, which will be confirmed by applying approaches similar to those of this study to future investigations.

5 Conclusion

In order to understand the formation process of microdolomite grains found within gas hydrate at an active gas chimney site, this study investigated their internal structures using polarizing microscopy, TEM, and STXM. The results reveal that dark and cloudy cores, and polygonal and isopachous external cements which are intrinsically different. The dark cores reflect heterogeneous nucleation on microbial EPS inside the hydrate microhabitats (Figure 4A). On the other hand, the cloudy core and isopachous external cement reflects homogeneous nucleation in relatively shallow depth where hydrate grew rapidly and dolomite nanocrystals accumulated on the surface of spherical oil films (Figure 4B). The polygonal external cement would reflect slow crystal growth in the deeper part, where the hydrate formation was less active. Thus, this study further strengthens the view that microdolomite is the product of interactions between methane, oil, and possibly microorganisms that have migrated upward through the sediments. Saline seep environments, such as submarine gas chimneys which host massive methane hydrate, provide the necessary conditions for the development of microdolomite grains similar to those we have observed and it is likely that similar grains exist in both presently active seep environments and are also preserved in fossil seep sites. This study revealed the characteristics of only two core-cement combinations, and while it is necessary to continue research into other types, hopefully our approach will provide a template for future investigation.

Data availability statement

The original contributions presented in the study are included in the article/supplementary material, further inquiries can be directed to the corresponding author.

Author contributions

RM and GS collected samples, FS, TA, NT, and YT conducted microscopic analyses, and all authors discussed ideas and wrote the manuscript.

Funding

This research was supported by the Japan Society for the Promotion of Science (JSPS) Grants-in-Aid for Scientific Research Nos. 21K18658 and 21K03739.

Acknowledgments

We acknowledge Dr. Shohei Yamashita for supporting STXM analyses. Two reviewers gave valuable and helpful suggestions and comments. The Joetsu Basin samples used in this study were collected by Meiji University's Gas Hydrate Research Laboratory under the commission of AIST (National Institute of Advanced Industrial Science and Technology) from 2013–2015 as part of the methane hydrate research project funded by METI (Ministry of Economy, Trade and Industry), Japan.

Conflict of interest

The authors declare that the research was conducted in the absence of any commercial or financial relationships that could be construed as a potential conflict of interest.

Publisher's note

References

Addadi, L., Raz, S., and Weiner, S. (2003). Taking advantage of disorder: Amorphous calcium carbonate and its roles in biomineralization. *Adv. Mat.* 15, 959–970. doi:10.1002/adma.200300381

Aoyama, C., Matsumoto, R., Okuda, Y., Ishida, Y., Hiruta, A., Sunamura, M., et al. (2004). Acoustical survey of methane plumes using the quantitative echo sounder in the eastern margin of the Sea of Japan, Oceans '04 MTS/IEEE Techno-Ocean '04 (IEEE Cat. No.04CH37600), Kobe. *Japan* 2, 1004–1009. doi:10.1109/OCEANS.2004.1405646

Bahniuk, A., McKenzie, J. A., Perri, E., Bontognali, T. R. R., Vögeli, N., Rezende, C. E., et al. (2015). Characterization of environmental conditions during microbial Mg-carbonate precipitation and early diagenetic dolomite crust formation: Brejo do Espinho, Rio de Janeiro, Brazil. *Geol. Soc. Lond. Spec. Publ.* 418, 243–259. doi:10.1144/sp418.11

Benzerara, K., Yoon, T. H., Tyliszczak, T., Constantz, B., Spormann, A. M., and Brown, G. E. (2004). Scanning transmission X-ray microscopy study of microbial calcification. *Geobiology* 2, 249–259. doi:10.1111/j.1472-4677.2004.00039.x

Black, J. G. (2005). *Microbiology: Principles and explorations*. Sixth ed. New York: Wiley & Sons.

Brandes, J. A., Wirick, S., and Jacobsen, C. (2010). Carbon K-edge spectra of carbonate minerals. *J. Synchrotron Radiat.* 17, 676–682. doi:10.1107/s0909049510020029

De Yoreo, J. J., and Vekilov, P. G. (2003). Principles of crystal nucleation and growth. *Rev. Mineral. Geochem.* 54, 57–93. doi:10.2113/0540057

De Yoreo, J. J., Gilbert, P. U. P. A., Sommerdijk, N. A. J. M., Penn, R. L., Whitelam, S., Joester, D., et al. (2015). Crystallization by particle attachment in synthetic, biogenic, and geologic environments. *Science* 349, 6760. doi:10.1126/science.aaa6760

Gilbert, P. U. P. A., Young, A., and Coppersmith, S. N. (2011). Measurement of c-axis angular orientation in calcite ($CaCO_3$) nanocrystals using x-ray absorption spectroscopy. *Proc. Natl. Acad. Sci. U. S. A.* 108, 11350–11355. doi:10.1073/pnas.1107917108

Gong, Y. U. T., Killian, C. E., Olson, I. C., Appathurai, N. P., Amasino, A. L., Martin, M. C., et al. (2012). Phase transitions in biogenic amorphous calcium carbonate. *Proc. Natl. Acad. Sci. U. S. A.* 109, 6088–6093. doi:10.1073/pnas.1118085109

Gunatilaka, A. (1989). Spheroidal dolomites – origin by hydrocarbon seepage? *Sedimentology* 36, 701–710. doi:10.1111/j.1365-3091.1989.tb02094.x

Hiruta, A., Snyder, G. T., Tomaru, H., and Matsumoto, R. (2009). Geochemical constraints for the formation and dissociation of gas hydrate in an area of high methane flux, eastern margin of the Japan Sea. *Earth Planet. Sci. Lett.* 279, 326–339. doi:10.1016/j.epsl.2009.01.015

Hiruta, A., Wang, L. C., Ishizaki, O., and Matsumoto, R. (2014). Last glacial emplacement of methane-derived authigenic carbonates in the Sea of Japan constrained by diatom assemblage, carbon-14, and carbonate content. *Mar. Pet. Geol.* 56, 51–62. doi:10.1016/j.marpetgeo.2014.04.005

Hitchcock, A. P. (2009). aXis2000 is written in interactive data language (IDL). Avaliable At: http://unicorn.mcmaster.ca/aXis2000.html.

James, N. P., and Jones, B. (2016). *Origin of carbonate sedimentary rocks*. Chichester: Wiley & Sons.

Li, H., and Estroff, L. A. (2007). Porous calcite single crystals grown from a hydrogel medium. *CrystEngComm* 9, 1153–1155. doi:10.1039/b709068d

Matsumoto, R., Okuda, Y., Hiruta, A., Tomaru, H., Takeuchi, E., Sanno, R., et al. (2009). Formation and collapse of gas hydrate deposits in high methane flux area of the Joetsu Basin, eastern margin of Japan sea. *J. Geogr.* 118, 43–71. doi:10.5026/jgeography.118.43

Matsumoto, R., Tanahashi, M., Kakuwa, Y., Snyder, G., Ohkawa, S., Tomaru, H., et al. (2017). Recovery of thick deposits of massive gas hydrates from gas chimney structures, eastern margin of Japan sea: Japan sea shallow gas hydrate project fire in the ice. Avaliable At: https://www.netl.doe.gov/sites/default/files/publication/MHNews-2017-Jan.pdf.

Metzler, R. A., Kim, W., Delak, K., Evans, J. S., Zhou, D., Beniash, E., et al. (2008). Probing the organic–mineral interface at the molecular level in model biominerals. *Langmuir* 24, 2680–2687. doi:10.1021/la7031237

Mitsunobu, S., Zhu, M., Takeichi, Y., Ohigashi, T., Suga, H., Jinno, M., et al. (2016). Direct detection of Fe(II) in extracellular polymeric substances (EPS) at the mineral-microbe interface in bacterial pyrite leaching. *Microbes Environ.* 31, 63–69. doi:10.1264/jsme2.me15137

Muramoto, K., Osawa, M., Kida, M., and Arisaka, H. (2007). A petroleum system in the deep water of the sado nanseioki area in the Japan sea based on the results of the MITI "sadooki nansei" seismic survey and the METI "sado nanseioki" wells. *J. Jpn. Assoc. Pet. Tech.* 72, 76–88. doi:10.3720/japt.72.76

Nguyen, B. T. T., Kido, M., Okawa, N., Fu, H., Kakizaki, S., and Imahori, S. (2016). Compaction of smectite-rich mudstone and its influence on pore pressure in the deepwater Joetsu Basin, Sea of Japan. *J. Mar. Pet. Geol.* 78, 848–869. doi:10.1016/j.marpetgeo.2016.07.011

Obst, M., Dynes, J. J., Lawrence, J. R., Swerhone, G. D. W., Benzerara, K., Karunakaran, C., et al. (2009). Precipitation of amorphous $CaCO_3$ (aragonite-like) by cyanobacteria: A STXM study of the influence of EPS on the nucleation process. *Geochim. Cosmochim. Acta* 73, 4180–4198. doi:10.1016/j.gca.2009.04.013

Perri, E., Tucker, M. E., Słowakiewicz, M., Whitaker, F., Bowen, L., and Perrotta, I. D. (2018). Carbonate and silicate biomineralization in a hypersaline microbial mat (Mesaieed sabkha, Qatar): Roles of bacteria, extracellular polymeric substances and viruses. *Sedimentology* 65, 1213–1245. doi:10.1111/sed.12419

Petrash, D. A., Bialik, O. M., Bontognali, T. R. R., Vasconcelos, C., Roberts, J. A., McKenzie, J. A., et al. (2017). Microbially catalyzed dolomite formation: From near-surface to burial. *Earth-Sci. Rev.* 171, 558–582. doi:10.1016/j.earscirev.2017.06.015

Politi, Y., Metzler, R. A., Abrecht, M., Gilbert, B., Wilt, F. H., Sagi, I., et al. (2008). Transformation mechanism of amorphous calcium carbonate into calcite in the sea urchin larval spicule. *Proc. Natl. Acad. Sci. U. S. A.* 105, 17362–17366. doi:10.1073/pnas.0806604105

Pouget, E. M., Bomans, P. H. H., Goos, J. A. C. M., Frederik, P. M., de With, G., and Sommerdijk, N. A. J. M. (2009). The initial stages of template-controlled $CaCO_3$ formation revealed by cryo-TEM. *Science* 323, 1455–1458. doi:10.1126/science.1169434

Roberts, J. A., Kenward, P. A., Fowle, D. A., Goldstein, R. H., González, L. A., and Moore, D. S. (2013). Surface chemistry allows for abiotic precipitation of dolomite at low temperature. *Proc. Natl. Acad. Sci. U. S. A.* 110, 14540–14545. doi:10.1073/pnas.1305403110

Sadooni, F. N., Howari, F., and El-Saiy, A. (2010). Microbial dolomites from carbonate-evaporite sediments of the coastal sabkha of Abu Dhabi and their exploration implications. *J. Pet. Geol.* 33, 289–298. doi:10.1111/j.1747-5457.2010.00480.x

Shiraishi, F., Hanzawa, Y., Okumura, T., Tomioka, N., Kodama, Y., Suga, H., et al. (2017). Cyanobacterial exopolymer properties differentiate microbial carbonate fabrics. *Sci. Rep.* 7, 11805. doi:10.1038/s41598-017-12303-9

Shiraishi, F., Omori, T., Tomioka, N., Motai, S., Suga, H., and Takahashi, Y. (2020). Characteristics of $CaCO_3$ nucleated around cyanobacteria: Implications for calcification process. *Geochim. Cosmochim. Acta* 285, 55–69. doi:10.1016/j.gca.2020.06.033

Snyder, G. T., Matsumoto, R., Suzuki, Y., Kouduka, M., Kakizaki, Y., Zhang, N., et al. (2020a). Evidence in the Japan Sea of microdolomite mineralization within gas hydrate microbiomes. *Sci. Rep.* 10, 1876. doi:10.1038/s41598-020-58723-y

Snyder, G. T., Sano, Y., Takahata, N., Matsumoto, R., Yoshihiro Kakizaki, Y., and Tomaru, H. (2020b). Magmatic fluids play a role in the development of active gas chimneys and massive gas hydrates in the Japan Sea. *Chem. Geol.* 535, 119462. doi:10.1016/j.chemgeo.2020.119462

Stumm, W., and Morgan, J. J. (1996). *Aquatic chemistry: Chemical equilibria and rates in natural waters*. New York: Wiley & Sons.

Tucker, M. E., and Wright, V. P. (1990). *Carbonate sedimentology*. Oxford: Blackwell.

Vasconcelos, C., and McKenzie, J. A. (1997). Microbial mediation of modern dolomite precipitation and diagenesis under anoxic conditions, Lagoa Vermelha, Rio de Janeiro, Brazil. *J. Sed. Res.* 67, 378–390. doi:10.1306/D4268577-2B26-11D7-8648000102C1865D

Vasconcelos, C., McKenzie, J. A., Bernasconi, S., Grujic, D., and Tien, A. J. (1995). Microbial mediation as a possible mechanism for natural dolomite formation at low temperatures. *Nature* 377, 220–222. doi:10.1038/377220a0

Warthmann, R., van Lith, Y., Vasconcelos, C., McKenzie, J. A., and Karpoff, A. M. (2000). Bacterially induced dolomite precipitation in anoxic culture experiments. *Geology* 28, 1091–1094. doi:10.1130/0091-7613(2000)028<1091:bidpia>2.3.co;2

Xu, Y., Tijssen, K. C. H., Bomans, P. H. H., Akiva, A., Friedrich, H., Kentgens, A. P. M., et al. (2018). Microscopic structure of the polymer-induced liquid precursor for calcium carbonate. *Nat. Commun.* 9, 2582. doi:10.1038/s41467-018-05006-w

Yin, X., Weitzel, F., Jiménez-López, C., Griesshaber, E., Fernández-Díaz, L., Rodríguez-Navarro, A., et al. (2020). Directing effect of bacterial extracellular polymeric substances (EPS) on calcite organization and EPS–carbonate composite aggregate formation. *Cryst. Growth Des.* 20, 1467–1484. doi:10.1021/acs.cgd.9b01113

Zhang, N., Lin, M., Snyder, G. T., Kakizaki, Y., Yamada, K., Yoshida, N., et al. (2019). Clumped isotope signatures of methane-derived authigenic carbonate presenting equilibrium values of their formation temperatures. *Earth Planet. Sci. Lett.* 512, 207–213. doi:10.1016/j.epsl.2019.02.005